



ZIF-67 incorporated with carbon derived from pomelo peels: A highly efficient bifunctional catalyst for oxygen reduction/evolution reactions



Hao Wang^{a,b}, Feng-Xiang Yin^{a,b,c,*}, Biao-Hua Chen^b, Xiao-Bo He^c, Peng-Liang Lv^a, Cai-Yun Ye^a, Di-Jia Liu^{d,**}

^a State Key Laboratory of Organic-Inorganic Composites, Beijing University of Chemical Technology, Beijing 100029, PR China

^b College of Chemical Engineering, Beijing University of Chemical Technology, Beijing 100029, PR China

^c Changzhou Institute of Advanced Materials, Beijing University of Chemical Technology, Changzhou 213164, Jiangsu, PR China

^d Chemical Sciences and Engineering Division, Argonne National Laboratory, Argonne, IL, 60439, USA

ARTICLE INFO

Article history:

Received 28 June 2016

Received in revised form 27 October 2016

Accepted 7 December 2016

Available online 8 December 2016

Keywords:

Metal-organic frameworks

Sustainable carbon

Synergistic effect

Bifunctional catalysis

ABSTRACT

Developing carbon catalyst materials using natural, abundant and renewable resources as precursors plays an increasingly important role in clean energy generation and environmental protection. In this work, N-doped pomelo-peel-derived carbon (NPC) materials were prepared using a widely available food waste—pomelo peels and melamine. The synthetic NPC exhibits well-defined porosities and a highly doped-N content (e.g. 6.38 at% for NPC-2), therefore affords excellent oxygen reduction reaction (ORR) catalytic activities in alkaline electrolytes. NPC was further integrated with ZIF-67 to form ZIF-67@NPC hybrids through solvothermal reactions. The hybrid catalysts show substantially enhanced ORR catalytic activities comparable to that of commercial 20 wt% Pt/C. Furthermore, the catalysts also exhibit excellent oxygen evolution reaction (OER) catalytic activities. Among all prepared ZIF-67@NPC hybrids, the optimal composition with ZIF-67 to NPC ratio of 2:1 exhibits the best ORR and OER bifunctional catalytic performance and the smallest ΔE ($E_{\text{OER}}@10 \text{ mA cm}^{-2}$ – $E_{\text{ORR}}@-1 \text{ mA cm}^{-2}$) value of 0.79 V. The catalyst also demonstrated desirable 4-electron transfer pathways and superior catalytic stabilities. The Co-N₄ in ZIF-67, electrochemical active surface area, and the strong interactions between ZIF-67 and NPC are attributed as the main contributors to the bifunctional catalytic activities. These factors act synergistically, resulting in substantially enhanced bifunctional catalytic activities and stabilities; consequently, this hybrid catalyst is among the best of the reported bifunctional electrocatalysts and is promising for use in metal-air batteries and fuel cells.

© 2016 Elsevier B.V. All rights reserved.

1. Introduction

Metal-organic frameworks (MOFs) are porous crystalline materials self-assembled with metal nodes and organic linkers with various compositions, high specific surface areas (SSAs), tuneable pore structures, and easily functionalised. Therefore, MOFs have provided opportunities for advancements in many research areas, including gas separation [1], drug delivery [2], catalysis [3], mag-

netism [4], and optoelectronics [5]. Most recently, MOF materials have been developed as electrocatalysts for the oxygen reduction reaction (ORR) and the oxygen evolution reaction (OER) [6–11], which are the two core reactions in many energy storage and conversion systems, including regenerative fuel cells and rechargeable metal-air batteries.

MOF-based materials as electrocatalysts for the ORR/OER are generally used in two ways. By self-sacrificing through pyrolysis, pristine MOFs can be converted into metal-based [12], metal-oxide-based [13] or carbon-based [14] materials. Such MOF-derived materials have been demonstrated to be active toward the ORR/OER but at the expense of the MOFs' properties. For instance, in most of cases, the specific surface areas of the Co-MOFs are reduced and their ordered porosities are destroyed [12]; both are disadvanta-

* Corresponding author at: State Key Laboratory of Organic-Inorganic Composites, Beijing University of Chemical Technology, Beijing 100029, PR China.

** Corresponding author.

E-mail addresses: yinfx@mail.buct.edu.cn (F.-X. Yin), djliu@anl.gov (D.-J. Liu).

geous for ORR/OER catalysis. Apart from their indirect uses, pristine MOFs can be used directly for ORR/OER [6,15–17]. Consequently, the active sites for ORR/OER not only can be directly designed and constructed during preparation but also can be well distributed within MOFs. Additionally, the highly developed porosities of MOFs aid in the diffusion of electrolytes and reactants and in the utilization of such catalytic sites. However, to date, when MOFs are used directly as electrocatalysts, their ORR/OER catalytic performance still falls short of meeting the practical application target; one of the main reasons for this shortcoming is their poor electronic conductivity. Supporting MOFs with porous carbon materials, such as activated carbon, graphene and their N-doped counterparts, is one of the most favourable strategies for solving this critical issue. Jahan et al. prepared pyridine-functionalised graphene to support Fe-porphyrin MOF as an ORR catalyst [18] and a copper-centred MOF integrated with graphene oxide as an ORR/OER catalyst [19]. Dramatically enhanced electrocatalytic performances were observed for the two MOF@carbon hybrids compared to that observed for the MOFs. The conductive nature of carbon materials facilitates the charge-transfer process, thus improving the catalytic activities of hybrids. In addition, carbon materials are involved in the building process of the composite and function as reinforcement fillers, strengthening the stabilities of the hybrids. Furthermore, the MOF and carbon work synergistically, resulting in greater catalytic efficiency.

The synthesis of carbon materials is conventionally based on fossil-fuel precursors and requires harsh synthetic conditions and high energy consumption [20]. Therefore, the introduction of sustainable concepts to obtain sustainable carbon materials has aroused great interest in recent years. Sustainable carbon materials are obtained using renewable resources such as food [21,22], insects [23], bacterial cellulose [24,25], and especially agriculture/food waste [26–28] as a carbon feedstock. These resources are renewable, cost-effective, high-quality, abundant and serving part of strategy for overall CO₂ reduction; in addition, the preparation processes are green and facile and are easy to scale up. Moreover, a large variety of novel carbon materials with prospects for practical application can be achieved [29]. To date, various agriculture/food wastes, including *Amaranthus* waste [30], pomelo peels [31–33], and *Typhaorientalis* [34], have been used to prepare nanostructured sustainable carbon materials to address the energy and environmental challenges. The recent pomelo-peel-derived carbon materials [31,33] not only show higher SSAs (>2100 m² g⁻¹) and better developed porosities than other biomass-derived carbon [35,36] but also show excellent specific capacitance, rate capability and cyclic stability in supercapacitors, highlighting their huge potential in energy storage and conversion applications.

Among materials in the MOF family, zeolitic imidazolate framework-67 (ZIF-67) possesses a relatively high nitrogen content [37]. The abundant Co-N₄ moieties are potentially favourable for both ORR [38] and OER [15] catalysis. On the basis of these considerations, we here synthesised N-doped pomelo-peel-derived carbon (NPC) through a pyrolysis method by using pomelo peels as a carbon source and melamine as a nitrogen source. The NPC samples afford excellent ORR catalytic activities in an alkaline electrolyte. After we integrated NPC with ZIF-67 through a solvothermal reaction, the ZIF-67@NPC hybrids not only showed considerably enhanced ORR catalytic activities and stabilities but also substantially improved OER catalytic activities and stabilities. In particular, the ZIF-67@NPC-2(2:1) sample, which features an optimal ZIF-67/NPC-2 mass ratio, exhibited superior overall bifunctional catalytic activity (with the smallest ΔE ($E_{\text{OER}}@10 \text{ mA cm}^{-2} - E_{\text{ORR}}@-1 \text{ mA cm}^{-2}$) value of 0.79). These results indicate that this material is among the best reported bifunctional ORR and OER catalysts.

2. Experimental

2.1. Preparation of the N-doped pomelo-peel-derived carbon samples

Guanxi honey pomelo was purchased from a local supermarket. The pomelo peels were cut into small pieces, washed with deionised water to remove dust and juice, and then dried at 80 °C for 3 days. The dried pomelo-peel pieces were ground into a fine powder. The powder was pre-carbonised at 400 °C under an N₂ flow to obtain pomelo-peel-derived carbon (PC). The resulting PC powder was soaked in 1 M KOH solution (with a KOH:PC mass ratio of 3:2), and the mixture was dried at 80 °C. The dried KOH-treated PC was subsequently ground with melamine (with a KOH-treated-PC:melamine mass ratio of 1:2), and the mixture was pyrolysed under an N₂ flow via the following procedure: the product was first heated to 450 °C, which was maintained for 30 min, and then increased to 650 °C and held for another 30 min; finally, the temperature was further increased to 800 °C and maintained at 800 °C for 1 h. Afterwards, the resulting product was soaked in 1 M HCl for 1 h and washed with deionised water to remove impurities, resulting in the NPC-2 sample. Other NPC samples with KOH-treated-PC:melamine mass ratios of 1:0.5, 1:1 and 1:4 were also synthesised via a similar procedure for comparison; these samples are hereafter denoted as NPC-0.5, NPC-1 and NPC-4, respectively.

2.2. Preparation of ZIF-67@NPC-2 samples

Cobalt(II) acetate (0.5 mmol) and 5 mmol of methyl-imidazole were dissolved into 4 mL of methanol separately under continuous magnetic stirring for several minutes. Then, 31 mg of NPC-2 was added to the 4 mL of methanol containing cobalt(II) acetate under continuous magnetic stirring for at least 1 h. The other 4 mL of methanol containing imidazole was then added dropwise into the reaction mixture. After stirring for 0.5 h, the resulting mixture was sealed in a Teflon-lined stainless steel autoclave, which was placed in an oven and heated from room temperature to 120 °C at a rate of 5 °C min⁻¹ and maintained at 120 °C for 24 h, followed by naturally cooling to room temperature. The obtained powder was washed with methanol several times and dried at 60 °C overnight. The final product is denoted as ZIF-67@NPC-2(2:1) (2:1 refers to the ZIF-67:NPC-2 mass ratio). ZIF-67@NPC-2 samples with ZIF-67:NPC-2 mass ratios of 1:1 and 1:2 were also synthesised via a similar procedure for comparison and are hereafter denoted as ZIF-67@NPC-2(1:1) and ZIF-67@NPC-2(1:2), respectively. Pure ZIF-67 was also synthesised via the same procedure used to prepare the ZIF-67@NPC-2 samples but in the absence of NPC-2. The ZIF-67 + NPC-2(2:1) mixture was obtained by physically mixing ZIF-67 with NPC-2 with a ZIF-67:NPC-2 mass ratio of 2:1.

2.3. Characterizations

The X-ray diffraction (XRD) patterns of the samples were recorded using a D/max-2500/PC X-ray diffractometer (Rigaku, Japan) equipped with a Cu-K α radiation source; the samples were scanned over the 2θ range from ~5 to 60°. The N₂ adsorption-desorption isotherms of the samples were collected using an Autosorb-iQ2-MP automatic analyser (Quantachrome, USA). The micropore-sized distributions of the samples were calculated via the Horvath-Kawazoe (H-K) method, and those of the mesopore-sized distributions were calculated by the Barrett-Joyner-Halenda (BJH) method. The specific surface areas (SSAs) were measured using the Brunauer-Emmett-Teller (BET) model. Field-emission scanning electron microscopy (FESEM) images of the samples were obtained using a SUPRA55 microscope (CARL ZEISS, Germany). Transmission electron microscopy

(TEM) images and high-resolution TEM (HRTEM) images of the samples were obtained using a JEM-2100 microscope (JEOL, Japan) and a Tecnai G2 F20 microscope (FEI, USA), respectively. The Raman spectra of the samples in the wavenumber range from 100 to 3500 cm^{-1} were recorded using a LabRAM ARAMIS (HORIBA JobinYvon, France) with a $\lambda = 532\text{ nm}$ laser. The ultraviolet-visible (UV-vis) spectra of the samples in ethanol ($\sim 2\text{ mg L}^{-1}$) were recorded using a UV-3600 spectrophotometer (Shimadzu, Japan). X-ray photoelectron spectroscopy (XPS) data were recorded using an ESCALAB 250 XPS instrument equipped with an Mg-K α X-ray source (Thermo, USA) at a pass energy 30 eV. The binding energy was calibrated by setting the C1s peak binding energy to 285.0 eV.

2.4. Electrochemical measurements

All electrochemical measurements were conducted at room temperature in 0.1 M KOH (pH = 13) using a rotating disk electrode (RDE) or a rotating ring-disk electrode (RRDE) apparatus (PINE, USA). The apparatus was connected to a computer-controlled CHI 760E electrochemical workstation (CH Instruments, China). The electrochemical measurements of the working electrodes were performed in a conventional three-electrode system. A KCl-saturated Ag/AgCl electrode and a Pt wire were used as the reference and counter electrodes, respectively. The KCl-saturated Ag/AgCl electrode was calibrated with respect to a reversible hydrogen electrode (RHE) by conducting cyclic voltammetry at a sweep rate of 1 mV s^{-1} on a Pt wire working electrode in H_2 -saturated 0.1 M KOH. The average of two potentials at which current crossed zero was regarded as the thermodynamic potential of hydrogen electrode reaction as shown in Fig. S1 ($E_{\text{RHE}} = E_{\text{Ag/AgCl}} + 0.953\text{ V}$). More details of the electrochemical performance tests and corresponding analysis are described in the supplementary data.

3. Results and discussion

3.1. Characterizations of the samples

A series of NPC samples with different nitrogen contents was synthesised by pyrolysis, where pomelo peels and melamine were used as the carbon and nitrogen sources, respectively. The PC and NPC samples exhibit similar XRD patterns (Fig. S1A), with no obvious difference. The two wide peaks at $\sim 23^\circ$ and $\sim 43^\circ$ 2θ are the (002) and (100) reflections of the disordered carbon layer, respectively [31]. Raman spectra demonstrate that all the NPC samples show a higher I_D/I_G value than PC due to the fact that the insertion of N atoms can cause distortion of sp^2 -carbon, resulting in higher degree of disorder and defect concentration than the pristine carbon material. The NPC-2 sample, with an additive KOH-treated-PC:melamine mass ratio of 1:2, exhibits the highest I_D/I_G value of 1.11, suggesting that NPC-2 has the highest degree of disorder and the highest defect concentration among the investigated NPC samples (Fig. S1B); both of these characteristics are considered beneficial for ORR/OER catalysis [39]. Therefore, NPC-2 was selected for integration with ZIF-67 through a solvothermal process. The XRD patterns of ZIF-67@NPC-2 with different ZIF-67/NPC-2 mass ratios are shown in Fig. 1A. The main XRD peak positions of the ZIF-67@NPC-2 samples match well with those of our synthetic pure ZIF-67 and also match well with those of the reported ZIF-67 (formula: $\text{Co}_3\text{C}_{24}\text{H}_{30}\text{N}_{12}$) [40], suggesting that ZIF-67 was successfully synthesised in the presence of NPC-2 through the solvothermal process. Additionally, a wide XRD peak at $\sim 23^\circ$ observed in pattern of each of the ZIF-67@NPC-2 samples corresponds to a disordered carbon layer in NPC-2, as previously mentioned.

Figs. 1 B and Fig. S2 show the N_2 adsorption-desorption isotherms of the samples. PC exhibits a combination of type-I and

type-IV isotherms based on IUPAC classification, suggesting that micropores and mesopores are predominant [41]. After N-doping, the isotherm of NPC-2 shows a negligible hysteresis loop and is a combination of type-I and type-II isotherms, suggesting that micropores and macropores are predominant. As summarised in Table S2, the BET SSA of NPC-2 is $1796\text{ m}^2\text{ g}^{-1}$, which is lower than that of PC ($2365\text{ m}^2\text{ g}^{-1}$); however, the pore volume of NPC-2 ($1.486\text{ cm}^3\text{ g}^{-1}$) is greater than that of PC ($1.278\text{ cm}^3\text{ g}^{-1}$). KOH is typically used as a micropore-forming agent to enrich porosities and increase the SSA in the preparation of sustainable carbon materials [42,43]. However, in this work, the SSA of NPC-2 did not increase but rather decreased after KOH was added. Generally, the additive KOH transforms into K_2CO_3 during the preparation. K_2CO_3 and the additive melamine decompose, generating a large amount of gas during pyrolysis. This large amount of released gas results in cracking of some of the micropores/mesopores, forming macropores. As a result, the NPC-2 exhibits a decreased SSA and an increased pore volume. The micropores provide a dense population of active sites, whereas macropores provide an easy mass-transfer path [44], both are beneficial for ORR/OER.

In the case of ZIF-67, the N_2 adsorption-desorption results indicate a relatively large quantity of adsorbed N_2 and a type-I adsorption isotherm, suggesting the presence of abundant micropores within the material. The three ZIF-67@NPC-2 hybrids show almost mixed type-I and type-II isotherms, also suggesting the presence of micropores, macropores, and very few mesopores (as confirmed by the pore size distributions in Fig. S3A-B). However, these three hybrids adsorb less N_2 than ZIF-67 and NPC-2. The BET SSAs of the ZIF-67@NPC-2 samples are also lower than those of NPC-2 and ZIF-67 (Table S2), which is due to the fact that in the hybrids NPC-2 slightly caused the distortion of ZIF-67, and ZIF-67 blocked some pores of NPC-2, resulting in lower SSAs [45,46]. With increasing NPC-2 content, the SSAs decrease in the order ZIF-67@NPC-2(2:1) ($1219\text{ m}^2\text{ g}^{-1}$) > ZIF-67@NPC-2(1:1) ($1024\text{ m}^2\text{ g}^{-1}$) > ZIF-67@NPC-2(1:2) ($828\text{ m}^2\text{ g}^{-1}$). Although all of the hybrids exhibit lower pore volumes than ZIF-67 and NPC-2, they still possess relative high pore volumes; furthermore, with variation in the NPC-2 content, the pore volumes of the hybrids change only slightly. Typically, high SSAs and large pore volumes favour high mass transfer and easy contact between reactants, catalytic sites and electrolyte in the ORR/OER.

The FESEM images in Fig. 2A indicate that PC is porous with many small pores distributed within the material; these pores are a consequence of the porous nature of pomelo peels. Fig. 2B depicts the morphology of NPC-2. Compared with PC, NPC-2 contains numerous loosely structured, tiny particles agglomerated into larger clusters, forming many large, accessible channels. These large channels are the macropores formed by the gas released by the KOH and melamine additives under high temperatures, as previously mentioned. This gas release increases the porosity (Fig. S2), which, in turn, reduces the mass-transport limitation. Fig. 2C shows the morphology of the ZIF-67@NPC-2(2:1) sample. In this sample, apart from the agglomerated small particles, which correspond to NPC-2, as previously mentioned, new small nanoparticles with a relatively smooth surface with an average size of 300–500 nm appear. The aforementioned XRD and reported results [39] indicate that the newly appeared nanoparticles in the form of dodecahedral morphology correspond to ZIF-67, indicating the successful formation of ZIF-67 in the presence of NPC-2 during the solvothermal process. The other two ZIF-67@NPC-2 samples also exhibit similar morphologies (Fig. S4). TEM and HRTEM were also performed on PC, NPC-2 and ZIF-67@NPC-2(2:1) to better understand their structures, and the observations on TEM are in good agreement with those on SEM. It is worth noting that the HRTEM image of ZIF-67@NPC-2(2:1) (Fig. 2c) shows the boundary of ZIF-67 and NPC-2, where they are partially interpenetrated, evidencing the intimate

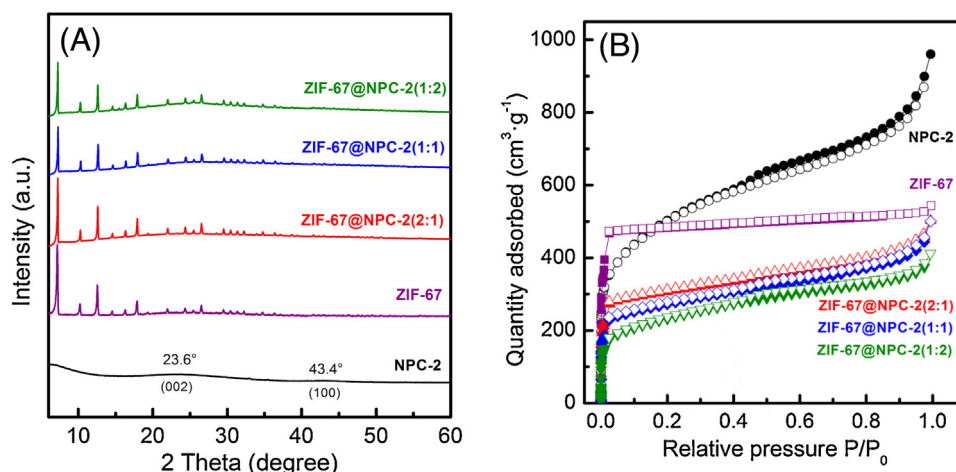


Fig. 1. (A) XRD patterns and (B) N₂ adsorption–desorption isotherms for the NPC-2, ZIF-67 and ZIF-67@NPC-2 samples.

Table 1

The N and Co atomic contents in ZIF-67 and ZIF-67@NPC-2 samples.

Samples	N 1s					Co 2p	
	N _{total}	N ₁ ^a	N ₂ ^b			Co _{total}	Co ³⁺ /Co ²⁺
			Pyridinic-	Pyrrolic-	Graphitic-		
ZIF-67	15.86	15.86	–	–	–	5.43	2.73
ZIF-67@NPC-2(2:1)	9.06	3.21	3.58	1.78	0.49	3.41	1.44
ZIF-67@NPC-2(1:1)	7.97	1.13	1.51	4.29	1.04	2.10	1.37
ZIF-67@NPC-2(1:2)	5.40	0.38	1.10	1.99	1.93	1.85	1.13

^a N₁ refers to Co-coordinated N in ZIF-67.

^b N₂ refers to N in NPC-2.

contact. Typically, ZIF-67 synthesised via solvothermal reaction exhibits a bulk particle morphology larger than 1 μm [38]. In this work, because of the presence of NPC-2 with a rough surface and the likely interactions generated in the solvothermal process between ZIF-67 and NPC-2, the ZIF-67 particles exhibit much smaller sizes.

The XPS results of the NPC samples with different amounts of added melamine are shown in Fig. S5 and Tables S3–4. According to the results in Table S3, the surface N content increases with increasing amount of melamine from NPC-0.5 to NPC-2 and then decreases from NPC-2 to NPC-4. Therefore, the NPC-2 possesses the highest surface N content of 6.38%. In NPC-2, the three fitted peaks located at 398.7, 400.4 and 401.4 eV are ascribed to pyridinic-, pyrrolic- and graphitic-N, respectively (Fig. 3A and Table S4) [34,47]. The single N 1s peak at 399.1 eV in ZIF-67 corresponds to Co-coordinated N [48]. After ZIF-67 was integrated with NPC-2, as shown in Fig. 3A, the Co-coordinated N peak in ZIF-67@NPC-2(2:1) changes slightly to 399.3 eV, whereas each of the other three N peaks in ZIF-67@NPC-2(2:1) change in the negative direction by 0.2–0.3 eV compared with those in the spectrum of NPC-2 (Table S4 and Table S7). The other two ZIF-67@NPC-2 hybrids also show a similar trend in the change of the N 1s energy binding compared with that in the spectrum of NPC-2. These results demonstrate that interactions occur between ZIF-67 and NPC-2. In the ZIF-67@NPC-2 hybrids, with increasing NPC-2 content, the total N content decreases and the N content contributed from ZIF-67 (N₁) also decreases (Table 1). Fig. 3B shows the deconvoluted Co 2p XPS spectra for the ZIF-67 and ZIF-67@NPC-2(2:1). In the spectrum of ZIF-67, the Co 2p_{3/2} peaks located at 781.3 eV, 782.9 eV and 786.5 eV represent Co³⁺, Co²⁺ and a satellite peak, respectively. These fitted individual peak positions are in good agreement with those reported in the literature [49]. Co³⁺ was transformed from outer Co²⁺ species of ZIF-67 through contact with gaseous oxygen [37]. After ZIF-67 was integrated with NPC-2, the binding energy of Co³⁺, Co²⁺ and the satellite

peak in ZIF-67@NPC-2(2:1) negatively decreased by 0.3, 0.2 and 0.1 eV, respectively, in comparison with those in the spectrum of pure ZIF-67 (Table S7). Shifts in the Co 2p binding energies are also observed in the spectra of the ZIF-67@NPC-2(1:1) and ZIF-67@NPC-2(1:2) hybrids compared with those in the spectrum of ZIF-67 (Table S7). These results suggest that different NPC-2 contents result in different electron binding abilities of Co ions in the hybrid materials [50], further confirming the existence of interactions between ZIF-67 and NPC-2 in the hybrids. Additionally, with decreasing ZIF-67 content in the ZIF-67@NPC-2 samples, the total Co content and the Co³⁺ proportion in total Co content decrease, whereas the Co²⁺ proportion increases (Table 1). The surface Co ion states in catalysts strongly affect their ORR/OER catalytic activities since Co²⁺ can be oxidised upon interaction with oxygen during ORR and Co³⁺ partially reduced during OER [37,51,52].

To further prove the existence of intimate contact and the resulting interactions between ZIF-67 and NPC-2 in the hybrid material, UV–vis adsorption spectra were recorded for NPC-2, ZIF-67, ZIF-67@NPC-2(2:1) and ZIF-67 + NPC-2(2:1) as shown in Fig. 3C. The pure ZIF-67 shows a characteristic band at 201.9 nm, and such a band is also observed on ZIF-67 + NPC-2(2:1) with the same wavelength, suggesting NPC-2 in the physical mixture has no effect on the structure of ZIF-67. However, NPC-2 in the ZIF-67@NPC-2(2:1) hybrid material causes a red shift of 6.1 nm in this absorption band compared with the pure ZIF-67. The red shift evidences the intimate contact, which leads to charge and energy transfer interactions between ZIF-67 and NPC-2.

3.2. Bifunctional catalytic performance of the samples

The ORR catalytic activities of the PC and NPC samples were examined in an RDE apparatus. As shown in Fig. S8, PC exhibited poor ORR catalytic activity, whereas after N-doping, the

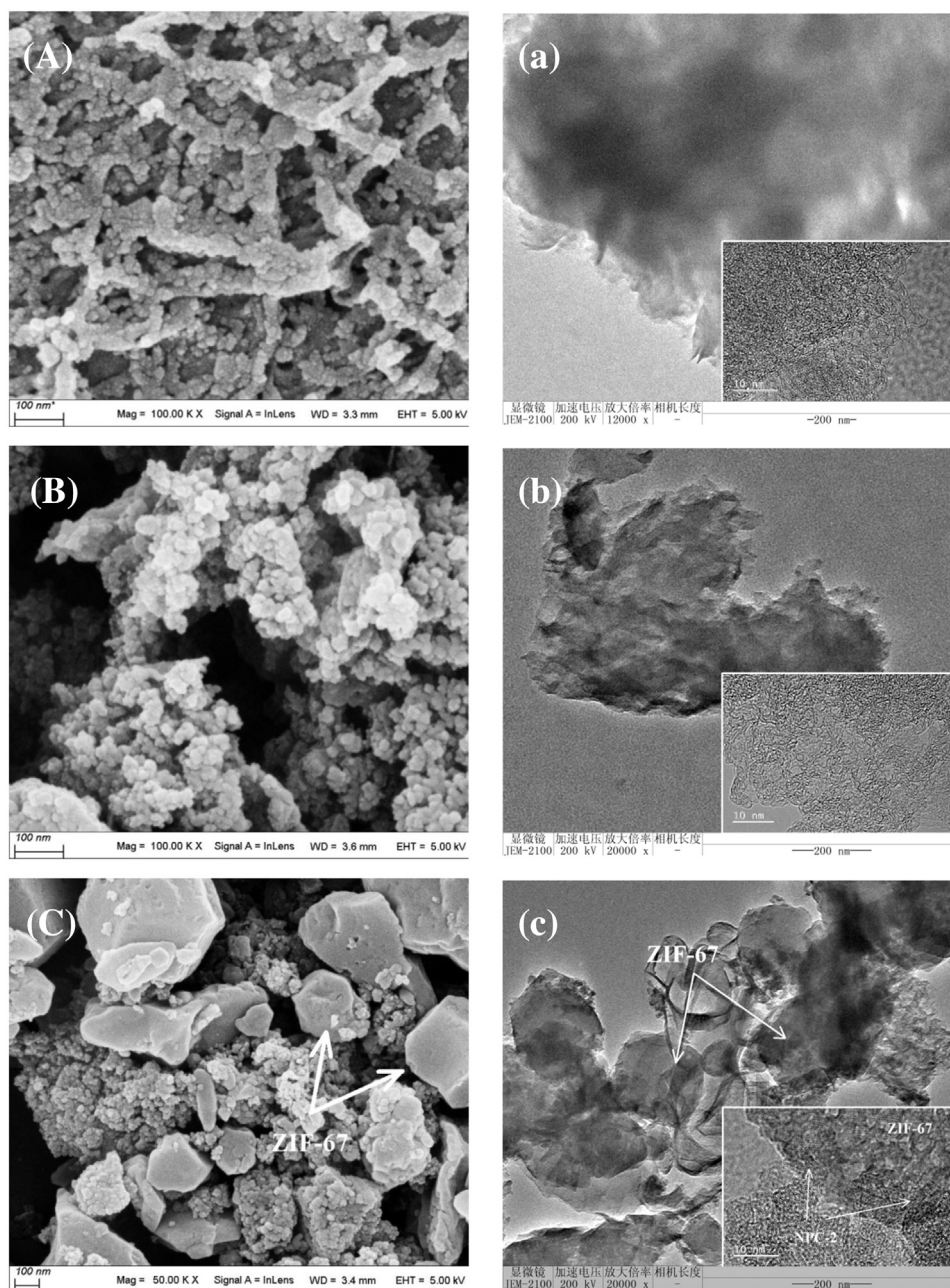


Fig. 2. (A–C) FESEM images of PC, NPC-2 and ZIF-67@NPC-2(2:1), respectively. (a–c) TEM images (inset: HRTEM images) of PC, NPC-2 and ZIF-67@NPC-2(2:1), respectively.

ORR catalytic activities of all of the NPC samples were considerably improved, suggesting that N-doping strongly alters the ORR catalytic activity of the pristine carbon materials. NPC-2, which contained the highest N content (Table S3 and Table S5), afforded the best ORR catalytic activity. The N dopant on carbon materials not only participates in ORR catalytic sites (pyridinic-/pyrrolic-N) [34,53,54], but also forms a large amount of short C–N bonds to improve the electronic conductivity of pristine carbon materials [55]. Additionally, compared to PC, NPC exhibits much better wettability (Fig. S6), which facilitates the ORR in aqueous electrolytes [31].

Fig. 4A compares the samples' ORR linear sweep voltammetry (LSV) curves collected at a sample rotation rate of 1600 rpm in O_2 -saturated 0.1 M KOH; the corresponding activity data are listed in Table 2. A commercial 20 wt% Pt/C sample was also tested under the same conditions as a reference. Interestingly, all of the ZIF-67@NPC-

2 samples show enhanced ORR catalytic activities compared to ZIF-67 and NPC-2 individually, likely as a consequence of the interactions between ZIF-67 and NPC-2. Among the ZIF-67@NPC-2 samples, the ORR activities in terms of the half-wave potential and the kinetic current density at 0.80 V decreased with increasing NPC-2 content (Table 2). ZIF-67@NPC-2(2:1) exhibited the best ORR catalytic activity, with an early half-wave potential of 0.82 V and a high kinetic current density of -4.97 mA cm^{-2} at 0.80 V. A comparison of ZIF-67@NPC-2(2:1) with 20 wt% Pt/C reveals that ZIF-67@NPC-2(2:1) exhibits a half-wave potential very similar to that of 20 wt% Pt/C (0.81 V) and outperforms 20 wt% Pt/C with respect to kinetic current density at 0.80 V (-4.97 mA cm^{-2} for ZIF-67@NPC-2(2:1) and -4.90 mA cm^{-2} for 20 wt% Pt/C), demonstrating the superior ORR catalytic activity of ZIF-67@NPC-2(2:1). Additionally, the ZIF-67@NPC-2(2:1) sample exhibits much higher ORR catalytic activity than the mechanical mixture (ZIF-67 + NPC-

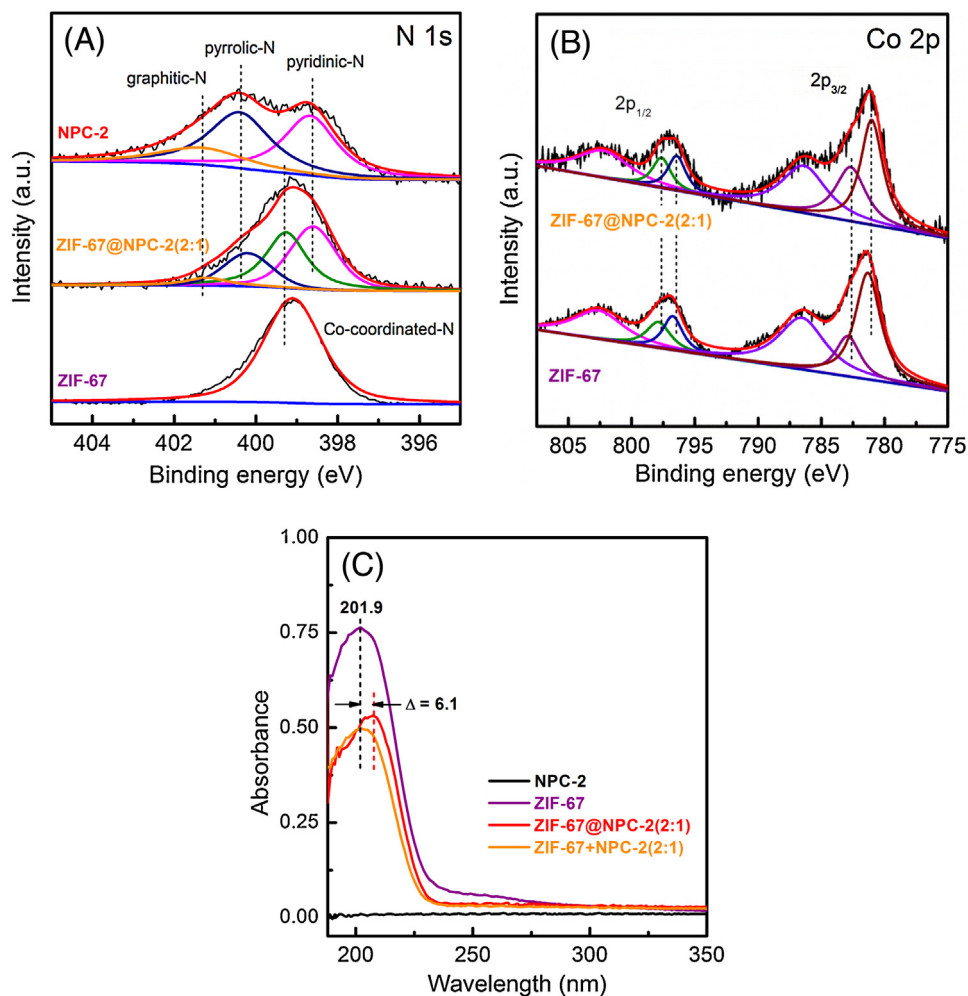


Fig. 3. (A) Deconvoluted N 1s spectra for NPC-2, ZIF-67 and ZIF-67@NPC-2(2:1). (B) Deconvoluted Co 2p spectra for ZIF-67 and ZIF-67@NPC-2(2:1). (C) UV-vis absorption spectra for NPC-2, ZIF-67, ZIF-67@NPC-2(2:1) and ZIF-67 + NPC-2(2:1).

Table 2

Bifunctional catalytic activities of the samples at 1600 rpm in O₂-saturated 0.1 M KOH.

Samples	ORR				OER		
	Potential (V) at −0.10 mA cm ^{−2}	Half-wave potential (V)	Kinetic current density at 0.80 V (mA cm ^{−2})	Diffusion- limiting current density (mA cm ^{−2})	Potential (V) at 10 mA cm ^{−2}	Half-wave potential (V)	Measured current density at 1.75 V (mA cm ^{−2})
NPC-2	0.86	0.74	−0.76	−4.34	–	–	0.93
ZIF-67	0.75	0.66	−0.01	−4.32	1.68	1.76	23.15
ZIF-67@NPC-2(2:1)	0.89	0.82	−4.97	−4.94	1.64	1.74	34.48
ZIF-67@NPC-2(1:1)	0.87	0.80	−3.07	−5.11	1.65	1.74	27.98
ZIF-67@NPC-2(1:2)	0.85	0.76	−0.89	−4.77	1.75	1.78	9.95
ZIF-67 + NPC-2(2:1)	0.86	0.76	−1.12	−5.22	1.67	1.75	27.82
20 wt% Pt/C	0.95	0.81	−4.90	−5.20	–	–	0.59

2(2:1)), demonstrating that the interactions between ZIF-67 and NPC-2 promote the ORR. To further verify the ability of the synergistic effect between ZIF-67 and NPC-2 to promote the ORR, we conducted electrochemical impedance spectroscopy (EIS), as shown in Fig. 8B, where the inset shows the equivalent circuit. The charge-transfer resistance (R_2) was determined to be 5.73 and 9.37 Ω for ZIF-67@NPC-2(2:1) and ZIF-67 + NPC-2(2:1), respectively. Apparently, the interaction between ZIF-67 and NPC-2 in the hybrid material minimises the charge-transfer resistance and facilitates the ORR, whereas the interaction between ZIF-67 and NPC-2 in the mechanical mixture does not. Some MOF@carbon

hybrids have already been developed as ORR catalysts. Compared with the graphene/Fe-porphyrin MOF also tested in 0.1 M KOH, our ZIF-67@NPC-2(2:1) exhibits an earlier half-wave potential shifted toward more positive potentials by approximately 300 mV [18].

The kinetic parameters of the ORR catalysed by the samples were analysed on the basis of the Tafel equation (Eq. S1), and the mass-corrected kinetic current density was introduced by considering the total mass of ZIF-67 and NPC-2. The corresponding Tafel curves are shown in Fig. 4B. The Tafel slopes associated with all of the ZIF-67@NPC-2 hybrids are smaller than that associated with NPC-2 (60 mV dec^{−1}), demonstrating the better ORR catalytic efficiency

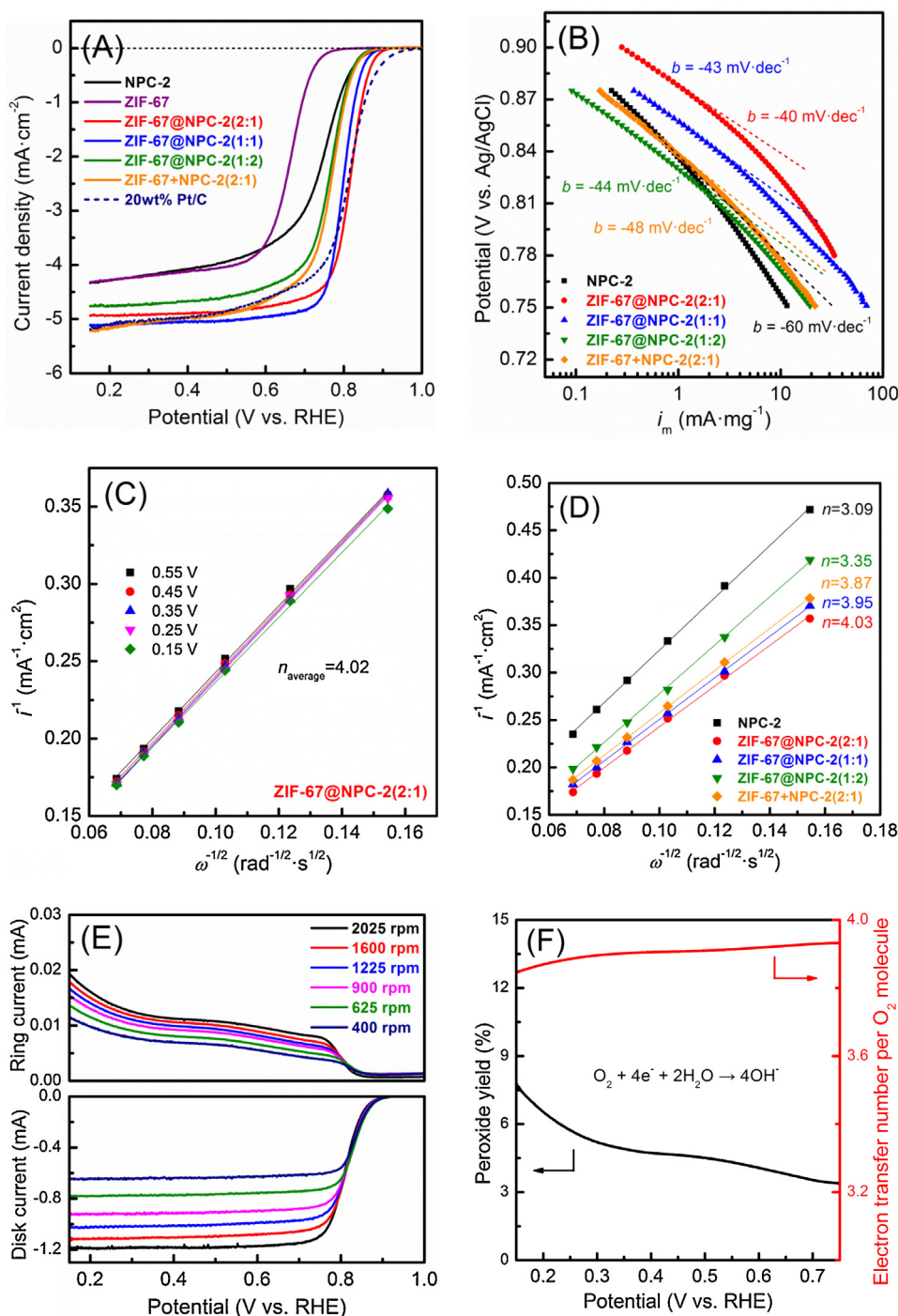


Fig. 4. (A) ORR LSV curves of the samples at an electrode rotation rate of 1600 rpm and a sweep rate of 5 mV s^{-1} . (B) Mass-corrected Tafel curves derived from their 1600 rpm ORR LSV curves. (C) Koutecky–Levich (K–L) curves of ZIF-67@NPC-2(2:1) at various potentials. (D) Comparison of the K–L curves of the samples at 0.55 V vs. RHE. (E) RRDE voltammograms at various electrode rotation speeds and a sweep rate of 5 mV s^{-1} for the ZIF-67@NPC-2(2:1) sample. (F) Peroxide yields and electron transfer number derived from the 1600 rpm RRDE voltammograms of ZIF-67@NPC-2(2:1).

of the hybrids. In the case of the ZIF-67@NPC-2 hybrid samples, the Tafel slopes increase with increasing NPC-2 content (40, 43, and 44 mV dec^{-1} for ZIF-67@NPC-2(2:1), ZIF-67@NPC-2(1:1), and ZIF-67@NPC-2(1:2), respectively). ZIF-67@NPC-2(2:1) exhibits the smallest Tafel slope of $2.3(2\text{RT}/3F)$, corresponding to 40 mV dec^{-1} ; this result suggests that the protonation of O_2^- on the active sites is the ORR rate-limiting step [56]. We also investigated the kinetic behaviour of pure ZIF-67, although it exhibited a sluggish ORR response. The Tafel slope of ZIF-67 was observed to be 50 mV dec^{-1} (within the potential range from 0.78 to 0.74 V vs. RHE). The Tafel

slopes of the ZIF-67@NPC-2 hybrids are more similar to the Tafel slope of ZIF-67 than to that of NPC-2, suggesting that ZIF-67 contributes more than NPC-2 to the ORR kinetics. Additionally, the Tafel slope of ZIF-67@NPC-2(2:1) is lower than that of the ZIF-67 + NPC-2(2:1) (48 mV dec^{-1}), suggesting that better ORR catalytic activity can be achieved through hybridization compared to that achieved through mechanical mixing.

The diffusion-controlled parameters of the sample-catalysed ORR process were analysed on the basis of the Koutecky–Levich equation shown in Eq. S2; the corresponding curves for the applied

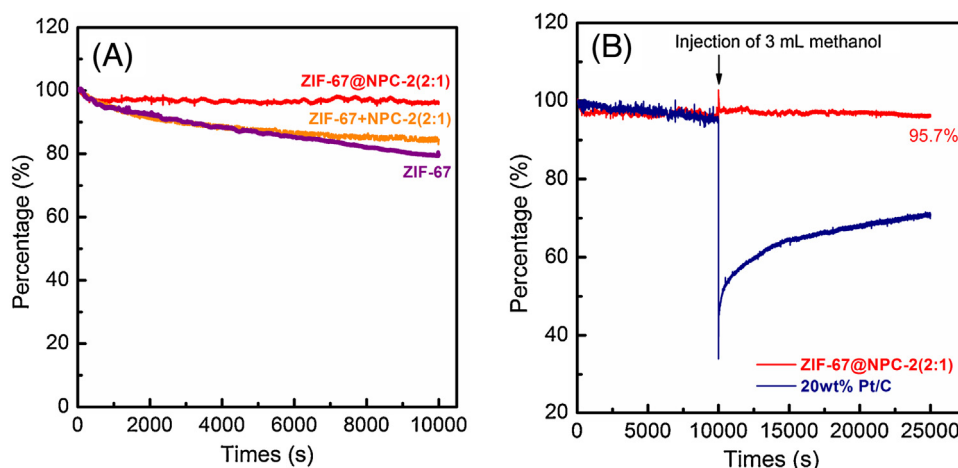


Fig. 5. (A) Chronoamperometric curves of percentage change in current density collected for the ZIF-67@NPC-2(2:1), ZIF-67 + NPC-2(2:1) and ZIF-67 samples in O_2 -saturated 0.1 M KOH at 0.55 V and at a rotational speed of 1600 rpm. (B) Methanol crossover tests were conducted by injecting 3 mL of methanol into test cells after 10,000 s for the ZIF-67@NPC-2(2:1) and 20 wt% Pt/C samples.

samples are illustrated in Fig. 4C–D and Fig. S9. In the case of the ZIF-67@NPC-2, ZIF-67 + NPC-2 and NPC-2 samples, i^{-1} exhibits a linear relationship with $\omega^{-1/2}$, demonstrating first-order reaction kinetics toward oxygen. In addition, they exhibit linear Koutecky–Levich (K–L) curves with nearly identical slopes under various potentials, which is indicative of the occurrence of a nearly identical oxygen reduction pathway on the samples. In particular, the ZIF-67@NPC-2 samples exhibit negligible gaps between their K–L curves (Figs. 4 C, Fig. S9a, b), suggesting completed kinetics on the ZIF-67@NPC-2 materials [57]. Fig. 4D compares the K–L curves of the applied samples at 0.55 V; the electron transfer numbers determined from K–L curves (Eq. S3) at 0.55 V are also shown in this figure. All ZIF-67@NPC-2 samples show lower K–L slopes and higher electron transfer numbers than NPC-2. Among the ZIF-67@NPC-2 hybrids, ZIF-67@NPC-2(2:1) possesses the smallest K–L slope and an electron-transfer number of 4.02, demonstrating its 4-electron ORR transfer pathway. The electron-transfer number of ZIF-67@NPC-2(2:1) is also higher than that of the mechanical mixture ($n = 3.87$). These results suggest that the ZIF-67 and NPC-2 work synergistically in the hybrid to afford greater catalytic efficiency.

Because of the superior catalytic properties of ZIF-67@NPC-2(2:1) among the ZIF-67@NPC-2 hybrids, its ORR mechanism was further studied using an RRDE apparatus with a Pt-ring electrode set at constant potential of 1.45 V. As shown in Fig. 4E, the ring current is two orders of magnitude less than the disk current. This negligible ring current indicates that the amount of HO_2^- intermediates generated during ORR is also negligible, suggesting high ORR catalytic efficiency. The electron transfer number and peroxide yields involved in the ZIF-67@NPC-2(2:1)-catalysed ORR process were determined from 1600 rpm RRDE voltammograms on the basis of Eqs. S9–10. As shown in Fig. 4F, within the applied potential range, less than 8% of the H_2O_2 reached the Pt ring, and the electron transfer numbers were determined to be 3.85–3.90, suggesting predominant direct 4-electron transfer pathway.

As reported, N and Co species are both regarded as catalytic sites for the ORR [58–60]. N, Co^{2+} and Co^{3+} species coexist in the synthetic ZIF-67@NPC-2 hybrids; thus, the hybrids have multiple catalytically active sites. In the case of N, as mentioned previously, pyridinic- and pyrrolic-N are generally regarded as active sites for the ORR [34,53,54]. According to Table 1, the ORR catalytic activities of the ZIF-67@NPC-2 hybrids follow the same order as the total content of pyridinic- and pyrrolic-N. Additionally, the ORR catalytic activities of the hybrids also follow the same order as the content of Co-coordinated N (N_1) in the hybrids, demonstrating that

the $Co-N_4$ coordination structures in ZIF-67 are also active centres. Surface Co^{2+} species rather than Co^{3+} species dominate the ORR [49,61]. However, in the ZIF-67@NPC-2 hybrids, the Co^{2+} proportion increases with increasing NPC-2 content; by contrast, the ORR catalytic activity shows the opposite trend, indicating that the Co^{2+} species are not the main contributor to the ORR. In the case of ORR, the SSA and pore volume also play key roles because a high SSA and high pore volume maximise the accessible region of catalytic sites, facilitate the transport of oxygen-related species, and permit easy contact between oxygen, catalytic sites and the electrolyte, thus promoting the ORR. According to Table S2, the pore volumes of the ZIF-67@NPC-2 samples change little; however, the ORR catalytic activities follow the same order as the SSAs of the samples. Furthermore, compared to the mechanical mixture, synergistic effects exist between ZIF-67 and NPC-2, which also facilitate ORR. These factors endow the hybrids with surprisingly high ORR catalytic activities.

Fig. 5A shows the catalytic ORR stabilities of the samples evaluated by chronoamperometry. Significantly, the current densities of the ZIF-67 and ZIF-67 + NPC-2(2:1) samples rapidly decay and stabilise at 79.8% and 84.4% of the initial values after 10,000 s, respectively. The ZIF-67@NPC-2(2:1) sample shows the smallest loss of initial activity and maintains a higher current density retention of 96.3% after 10,000 s. Along with catalytic stabilities, tolerance to methanol crossover is also critical for ORR catalysts when they are used for direct methanol fuel cell. After 10,000 s of chronoamperometry tests, 3 mL of methanol was injected into the test cell and the chronoamperometry tests were continued for another 15,000 s. In addition, 20 wt% Pt/C was also examined under the similar condition as a comparison. As shown in Fig. 5B, methanol poisoning negligibly affected the ORR current density of the ZIF-67@NPC-2(2:1) hybrid, which retained 95.7% of its initial ORR current density. However, there is a large decrease of current density percentage for 20 wt% Pt/C upon the added methanol mainly due to the active response of Pt towards methanol oxidation, thus affecting ORR [62]. After a 25,000 s chronoamperometry stability test in the presence of methanol, the ORR LSV curve of the ZIF-67@NPC-2(2:1) at 1600 rpm was recorded again (Fig. S10). The hybrid showed only a 10 mV reduction in its half-wave potential and retained 96% of its initial current density at 0.55 V, also demonstrating the excellent stability of the ZIF-67@NPC-2(2:1) sample. This excellent activity stability likely results from the interactions between ZIF-67 and NPC-2, which stabilise the catalytically active sites in the ZIF-67@NPC-2(2:1) sample.

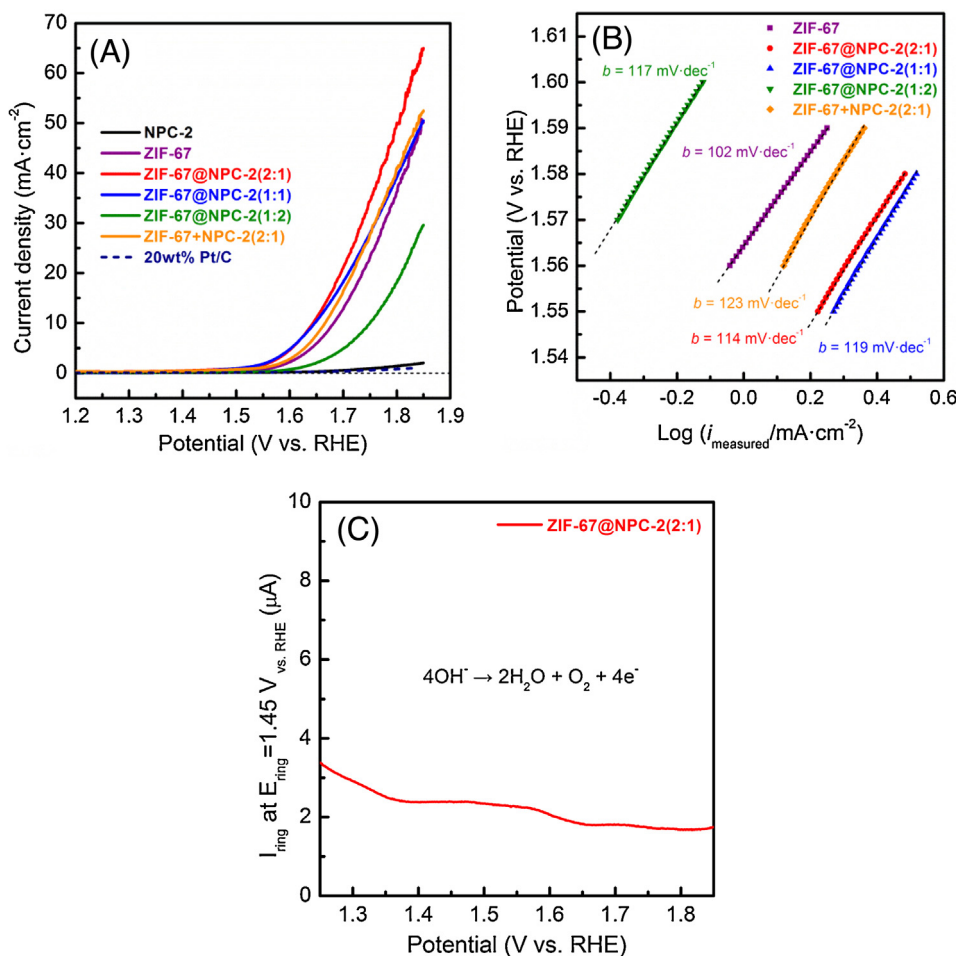


Fig. 6. (A) OER LSV curves at 1600 rpm with a sweep rate of 5 mV s⁻¹. (B) OER Tafel curves derived from 1600 rpm OER LSV curves of the samples. (C) Ring current or detection of H₂O₂ generated from a disk electrode with the potential of the Pt-ring electrode fixed at 1.45 V vs. RHE.

The catalytic activities of the NPC samples toward the OER were also examined in an RDE apparatus. As shown in Fig. S11, compared to PC, all of the NPC samples exhibited improved OER catalytic activities, although the improvements were limited. The doped-N atoms from melamine in NPC, which are in the form of pyrrolic- and pyrrolic-N, are regarded as ORR catalytic sites but contribute little to the OER. After N doping, the large amount of C-N species improves the electronic conductivity of NPC and therefore accounts for the improvements in the OER on NPC compared to that on PC.

The OER activities of the ZIF-67@NPC-2, NPC-2, ZIF-67 samples are illustrated in Fig. 6A; the corresponding data are also summarised in Table 2. As observed, NPC-2 and 20 wt% Pt/C exhibited a poor OER catalytic response. By contrast, the ZIF-67 and ZIF-67@NPC-2 samples exhibited much higher OER catalytic activities. In the case of the ZIF-67@NPC-2 hybrids, the sample with a lower NPC-2 content exhibited higher OER catalytic activity. At a current density of 10 mA cm⁻², ZIF-67@NPC-2(2:1) and ZIF-67@NPC-2(1:1) exhibited similar overpotentials (Eq. S5) of ~0.41 V, which is comparable with the overpotentials of the best reported Co-based/N-doped-carbon hybrid catalysts, such as Co_xO_y/NC (0.43 V) [63] and N-Co-doped PCP//NRGO (0.43 V) [39]. Although ZIF-67@NPC-2(1:1) exhibited OER catalytic behaviour similar to that of ZIF-67@NPC-2(2:1) at potentials less than 1.65 V, the former failed to deliver a higher current density at 1.75 V (27.98 mA cm⁻²) than the latter (34.48 mA cm⁻²). The ZIF-67@NPC-2(1:2) exhibited inferior catalytic activity compared to that of ZIF-67 because the ZIF-67 mass content in ZIF-67@NPC-2(1:2) was

only one-third of that in pure ZIF-67 in the prepared working electrodes (Table S1). Fig. 6A compares the OER catalytic activity of ZIF-67@NPC-2(2:1) with that of the mechanical mixture (ZIF-67 + NPC-2(2:1)). ZIF-67@NPC-2(2:1) exceeds ZIF-67 + NPC-2(2:1) completely for OER catalysis, suggesting that the synergistic effects between ZIF-67 and NPC-2 also promote the OER catalytic performance of the hybrid.

The OER kinetic performance of the samples was also analysed on the basis of the Tafel equation. As shown in Fig. 6B, to deliver a given current density, ZIF-67@NPC-2(2:1) and ZIF-67@NPC-2(1:1) may require similarly smaller overpotentials compared to those required for the other samples. ZIF-67 exhibits the smallest Tafel slope (102 mV·dec⁻¹) among the investigated samples but shows a large OER overpotential. This result demonstrates that, although the Co-N₄ structures in ZIF-67 are beneficial for OER kinetics, the lack of carbon in ZIF-67 results in inferior charge-transfer characteristics. Each of the ZIF-67@NPC-2 hybrids shows a smaller Tafel slope (114, 119 and 117 mV·dec⁻¹ for ZIF-67@NPC-2(2:1), ZIF-67@NPC-2(1:1) and ZIF-67@NPC-2(1:2), respectively) than the mechanical mixture (123 mV·dec⁻¹), suggesting that the interactions between ZIF-67 and NPC-2 in the hybrids enhance the OER kinetics. ZIF-67@NPC-2(2:1) exhibits the smallest Tafel slope among all of the investigated ZIF-67@NPC-2 hybrids, demonstrating its superior OER kinetics. The Tafel slope of NPC-2 (252 mV·dec⁻¹ within the potential range of 1.72–1.75 V vs. RHE) is almost double that of each hybrid, suggesting that the Co-N₄ centres in ZIF-67 dominate the OER kinetics.

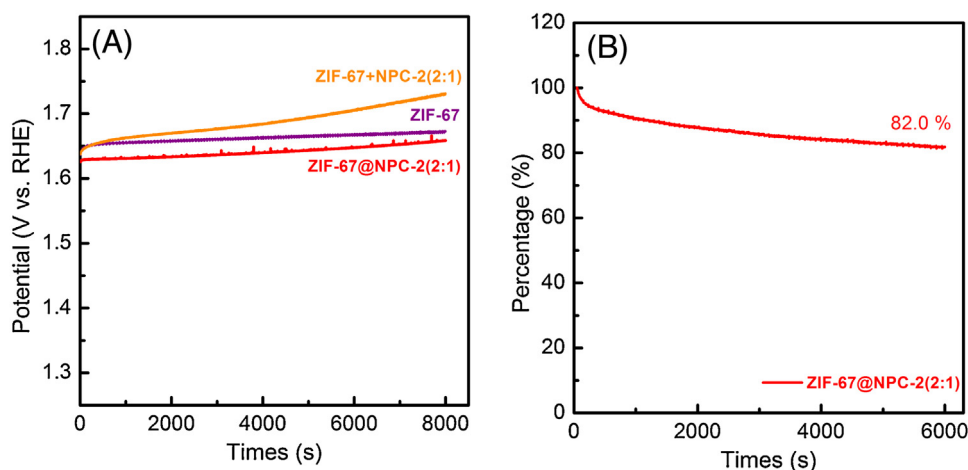


Fig. 7. (A) Chronopotentiometric curves for the ZIF-67@NPC-2(2:1), ZIF-67 and ZIF-67 + NPC-2(2:1) samples in O_2 -saturated 0.1 M KOH with the anodic current density fixed at 5 mA cm^{-2} and the rotation speed fixed at 1600 rpm. (B) Chronoamperometric curve for the ZIF-67@NPC-2(2:1) sample in O_2 -saturated 0.1 M KOH with the anodic potential fixed at 1.55 V and the rotation speed fixed at 1600 rpm.

ZIF-67@NPC-2(2:1), as the best OER catalyst among the studied samples, was subsequently electrochemically characterised by RRDE to elucidate its OER catalytic mechanism. As shown in Fig. 6C, the ring current was negligible, indicating that few hydrogen peroxides were generated from the disk electrode, suggesting a desirable 4-electron transfer pathway involved in the ZIF-67@NPC-2(2:1)-catalysed OER process [64]. The electron transfer number, 4, was then used to calculate the turnover frequency (TOF) for the samples. On the basis of Eq. S6, the TOFs of the ZIF-67@NPC-2(2:1) and ZIF-67 + NPC-2(2:1) samples were determined to be 0.013 and 0.009 s^{-1} , respectively. The ZIF-67@NPC-2(2:1) exhibits a TOF higher than that reported for $\text{Co}(\text{OH})_2$ (0.004 s^{-1}) measured in 1 M KOH [65], demonstrating the superior OER catalytic performance of our synthetic hybrid.

The surface Co^{3+} species dominate the OER catalytic activity because Co^{3+} sites aid in electrophilic adsorption and are beneficial for the conversion of OH^- into oxygen [51]; in addition, the extraction of O during the OER process is believed to occur predominantly at Co^{3+} sites [66]. The OER catalytic activities of the hybrids follow the order of the $\text{Co}^{3+}/\text{Co}^{2+}$ ratio in the samples, confirming that Co^{3+} is involved in the catalysis. According to the correlation between the OER catalytic activity and the ZIF-67 content in the hybrids, Co-N_4 centres in ZIF-67 are active toward OER under alkaline conditions. These results demonstrate that the hybrids are active OER materials with multiple catalytic sites. Additionally, the OER catalytic activities of the ZIF-67@NPC-2 samples also follow the same order of the SSAs of the samples. The interactions between ZIF-67 and NPC-2 facilitate fast charge transfer of the hybrids. Therefore, the surface Co species, SSAs, and interactions between ZIF-67 and NPC-2 work synergistically in determining the OER catalytic activities of the hybrids.

The OER activity stabilities of the ZIF-67, ZIF-67@NPC-2(2:1) and ZIF-67 + NPC-2(2:1) samples were first examined by chronopotentiometry. As shown in Fig. 7A, at a constant current density of 5 mA cm^{-2} , the OER potentials for ZIF-67@NPC-2(2:1) and ZIF-67 remained very stable, with increases of only 33 mV and 36 mV, respectively. Meanwhile, the OER overpotential of the ZIF-67 + NPC-2(2:1) sample rapidly increased by 93 mV after 8000 s. ZIF-67@NPC-2(2:1) exhibited the lowest overpotential among the investigated materials. These results are in good agreement with the OER catalytic activity results. The ZIF-67@NPC-2(2:1) was subsequently examined by chronoamperometry at a constant potential of 1.55 V and at an electrode rotation rate of 1600 rpm to further investigate its OER catalytic stability. As shown in Fig. 7B, after

6000 s, 82.0% of its initial OER current was maintained, which is better than the results previously reported for a novel ZIF-67-derived catalyst [39]. In the ZIF-67@NPC-2(2:1) sample, the synergistic effects between ZIF-67 and NPC-2 enhance the OER stability of the hybrid.

On the basis of the aforementioned results, the ZIF-67@NPC-2(2:1) sample not only exhibited the best ORR but also the best OER catalytic activity; this material thus affords the best overall bifunctional catalytic activity among the samples investigated in this work. The ΔE ($E_{\text{OER}}@10 \text{ mA cm}^{-2} - E_{\text{ORR}}@-1 \text{ mA cm}^{-2}$) is a critical criterion for assessing the overall bifunctional catalytic activity of a catalyst. A lower value represents better overall bifunctional catalytic activity. The ΔE value of the ZIF-67@NPC-2(2:1) sample was observed to be 0.79 V, which is comparable with the values reported for recently developed precious metal catalysts, MOF-derived composites, and transition-metal oxides, as listed in Table 3 (more in Table S9). We also believe that using a KOH-treated NPC-2 rather than a NPC_{withoutKOH}-2 as ZIF-67 support shows the merits, and further studies were conducted by investigating the morphology and bifunctional catalytic activities of ZIF-67@NPC_{withoutKOH}-2(2:1). As shown in Fig. S12, ZIF-67 formed on NPC_{withoutKOH}-2 shows larger average particle size ($\sim 1 \mu\text{m}$) than on NPC-2 (300–500 nm). Large sized particles deteriorate the bifunctional catalytic activities.

Generally, the catalytic sites for ORR and OER differ. In ZIF-67@NPC-2 hybrids, the pyridinic-N, pyrrolic-N and Co-N_4 are the ORR catalytic sites, whereas the Co^{3+} and Co-N_4 are the OER catalytic sites. However, the ZIF-67@NPC-2(2:1) sample affords the best ORR and OER catalytic activities simultaneously. According to the kinetics results, Co-N_4 contributes to both the ORR and the OER and dominates the two reactions. Thus, Co-N_4 plays a key role in determining the bifunctional catalytic activities of the ZIF-67@NPC-2 hybrids. On the basis of the aforementioned results, the SSA and the interactions between ZIF-67 and NPC-2 also critically affect the two reactions. Although the hybrids exhibit high SSAs and the ORR/OER catalytic activity of the hybrids follows the same order as the SSA, the electrocatalytic activity of a catalyst should be directly associated with its electrochemically active surface area (EASA) [69,70]. Therefore, we conducted CV experiments in an RDE apparatus to measure the double-layer capacitance (C_{DL}), which provides information related to the EASA. According to Eq. S8, the EASA is proportional to the C_{DL} and a higher C_{DL} represents a higher EASA in the catalyst (Eqs. S7–8). The detailed procedures are described in the supplementary data; the obtained CV curves in a small potential range from 0.90 to 1.00 V vs. RHE for the samples

Table 3Bifunctional activity comparisons of the ZIF-67@NPC-2(2:1) sample with the reported novel bifunctional catalysts at 1600 rpm in O₂-saturated 0.1 M KOH.

Samples	$E_{\text{ORR}}/V_{\text{vs.RHE}} @ -1 \text{ mA cm}^{-2}$	$E_{\text{OER}}/V_{\text{vs.RHE}} @ 10 \text{ mA cm}^{-2}$	$\Delta E/V(E_{\text{ORR}}-E_{\text{OER}})$	Ref.
ZIF-67@NPC-2(2:1)	0.85	1.64	0.79	This work
20 wt% Ir/C	$\sim 0.79^a$	1.61	0.82	[67]
N/Co-doped PCP	$\sim 0.89^a$	1.75	1.02	[39]
Z-9-800-250	$\sim -0.10^{a,b}$	$\sim 0.78^b$	0.88	[68]
Co _x O _y /NC	0.80	1.66	0.86	[63]

^a “~” indicates that the values were read directly from figures in the corresponding papers.^b The potentials are relative to Ag/AgCl reference electrode.

are shown in Fig. 8A and Fig. S13. By calculating the slope of the linear relationship between the current density and the scan rate, we determined that the C_{DL} values of ZIF-67, ZIF-67@NPC-2(2:1), ZIF-67@NPC-2(1:1), ZIF-67@NPC-2(1:2) and ZIF-67 + NPC-2(2:1) were 1.208, 1.261, 1.132, 0.629 and 0.809 mF, respectively. The C_{DL} exhibited the same trend as the ORR/OER catalytic activity in the ZIF-67@NPC-2 hybrids, and ZIF-67@NPC-2(2:1) exhibited the highest C_{DL} . Notably, ZIF-67 exhibited a C_{DL} comparable with those of ZIF-67@NPC-2(2:1) and ZIF-67@NPC-2(1:1) but exhibited inferior bifunctional catalytic activity compared to these two samples. These results suggest that ZIF-67 has a high EASA, but because it lacks NPC-2, ZIF-67 fails to deliver high current density. ZIF-67@NPC-2(2:1) also exhibited a higher C_{DL} than the mechanical mixture, suggesting that the combination creates more available EASAs for electrocatalysis.

As previously mentioned, interactions occur between ZIF-67 and NPC-2 in the hybrids. These interactions may result in tight contact between the two species, which would further enhance the charge-transfer properties. To investigate such properties, we conducted EIS; the details are presented in the supplementary data. As shown in Fig. 8B, the complex plane plots of the ZIF-67@NPC-2 hybrids exhibit a smaller semicircle diameter than those of the mechanical mixture and pure ZIF-67. These results indicate that the electronic conductivity of ZIF-67@NPC-2 was markedly enhanced after integration with NPC-2. The inset of Fig. 8B shows the equivalent circuit, in which R_1 and R_2 represent the solution resistance (R_s) and the charge-transfer resistance (R_{ct}), respectively. The charge-transfer resistances of ZIF-67, ZIF-67@NPC-2(2:1), ZIF-67@NPC-2(1:1), ZIF-67@NPC-2(1:2) and ZIF-67 + NPC-2(2:1) were observed to be 18.54, 5.73, 5.68, 5.95 and 9.37 Ω , respectively. ZIF-67@NPC-2(2:1) exhibits relatively low charge-transfer resistance, demonstrating its excellent conductivity. The apparent lower impedance of the ZIF-67@NPC-2 hybrids compared to the mechanical mixture indicates that the strong interactions between ZIF-67

and NPC-2 in the hybrid materials form a tight contact and thus can form a faster charge-transfer pathway [71]. Although catalytic sites for ORR and OER differ, on the basis of the aforementioned analysis, Co-N₄, EASA and interactions between ZIF-67 and NPC-2 are the main contributors to both the ORR and the OER, governing the bifunctional catalytic activities of the hybrids. The ZIF-67@NPC-2(2:1), which exhibits the highest Co-N₄ content, the highest EASA, and the strongest interactions, affords the best ORR and OER catalytic activity and, thus, the best overall bifunctional catalytic activities.

Based on the aforementioned results, the ORR catalytic activities of the hybrids follow the order as the content of Co-coordinated N in the hybrids, and Co-N₄ centres in ZIF-67 are also active toward OER according to the correlation between the OER catalytic activity and the ZIF-67 content in the hybrids, demonstrating that the Co-N₄ coordination structures in ZIF-67 are active centres for ORR/OER. Additionally, the double-layer capacitance, which is proportional to EASA, exhibited the same trend as the ORR/OER catalytic activity in the ZIF-67@NPC-2 hybrids, and integration of ZIF-67 and NPC-2 (ZIF-67@NPC-2(2:1)) creates more EASAs than the physical mixture (ZIF-67 + NPC-2(2:1)) for ORR/OER. Furthermore, tight contact between ZIF-67 and NPC-2 in the hybrids results in interactions, which further enhance the charge and energy transfer properties, facilitating ORR/OER. By comparing ZIF-67@NPC-2(2:1) with NPC-2, ZIF-67 and ZIF-67 + NPC-2(2:1), it is easy to find that NPC-2 shows limited bifunctional catalytic activities due to the absence of Co-N₄ sites; ZIF-67, which has abundant Co-N₄ sites and a high EASA, still shows inferior bifunctional catalytic activities to ZIF-67@NPC-2(2:1) since it lacks carbon materials and therefore fails to deliver high current density; and even ZIF-67 + NPC-2(2:1), a physical mixture that contains both ZIF-67 and NPC-2, still affords lower bifunctional catalytic activities than ZIF-67@NPC-2(2:1) due to the fact that ZIF-67 and NPC-2 in the physical mixture lack intimate contact and cannot create a high EASA and effective interactions to

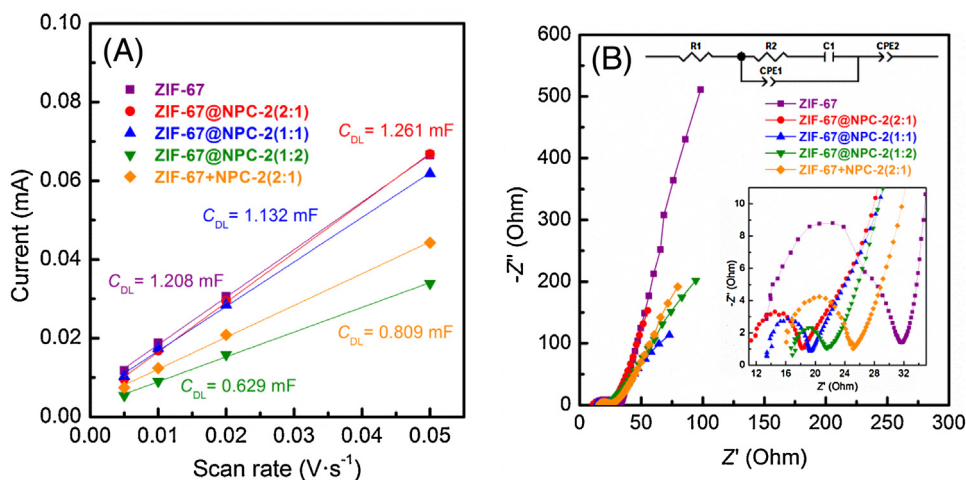


Fig. 8. (A) Plots of the current density at 0.95 V vs. scan rate. (B) EIS recorded at an open-circuit potential for the ZIF-67@NPC-2 samples and for the mechanical mixture ZIF-67 + NPC-2(2:1) (inset: the corresponding equivalent circuit diagram).

facilitate charge transfer. Therefore, the Co-N₄ in ZIF-67, EASA, and the interactions between ZIF-67 and NPC-2 are the main contributors to the bifunctional catalytic activities, and these factors act synergistically and are indispensable to make ZIF-67@NPC-2(2:1) among the best of the reported bifunctional electrocatalysts in alkaline electrolytes.

4. Conclusions

A series of NPC catalysts were synthesised through pyrolysis using widely available and renewable pomelo peels as the carbon source and melamine as the nitrogen source. The NPC precursor exhibited a high SSA, abundant micropores/macropores, a large amount of pyridinic-/pyrrolic-N sites, and, therefore, excellent ORR catalytic activity. When NPC was integrated with ZIF-67, all of the resulting synthetic ZIF-67@NPC-2 hybrids afforded excellent ORR and OER catalytic performance. In the hybrids, the Co-N structures in ZIF-67 and the N species in NPC-2 were observed to be responsible for the ORR; the Co-N structures and Co³⁺ species were observed to be responsible for the OER, whereas the EASA and strong interactions between ZIF-67 and NPC-2 were favourable to both the ORR and the OER. Among the hybrids, ZIF-67@NPC-2(2:1) exhibited not only the best ORR catalytic performance—even better than that of 20 wt% Pt/C, with a much earlier half-wave potential of 0.82 V and better catalytic stability—but also the best OER catalytic performance, with a small overpotential of 0.41 V at 10 mA cm⁻² and excellent catalytic stability. Therefore, ZIF-67@NPC-2(2:1) exhibited the best overall bifunctional catalytic activity (ΔE value of 0.79), which was mainly a consequence of its highest content of Co-N₄ moieties in ZIF-67, highest EASA, and strong interactions between ZIF-67 and NPC-2, ranking it among the best bifunctional non-precious-metal electrocatalysts. In this work, we integrated MOFs with sustainable carbon and obtained a highly effective bifunctional catalyst, opening a new route for MOFs in electrocatalysis.

Acknowledgements

We gratefully acknowledge the Natural Science Foundation of China (Project No. 21276018), the Fundamental Research Funds for the Central Universities (Project No. buctrc201526), the Changzhou Sci & Tech Program (Project No. CJ20159006), and the Advanced Catalysis and Green Manufacturing Collaborative Innovation Centre of Changzhou University.

Appendix A. Supplementary data

Supplementary data associated with this article can be found, in the online version, at <http://dx.doi.org/10.1016/j.apcatb.2016.12.016>.

References

- [1] Q. Yang, D. Liu, C. Zhong, J.-R. Li, *Chem. Rev.* 113 (2013) 8261–8323.
- [2] P. Horcajada, C. Serre, M. Vallet-Regí, M. Sebban, F. Taulieu, G. Férey, *Angew. Chem.* 118 (2006) 6120–6124.
- [3] J. Lee, O.K. Farha, J. Roberts, K.A. Scheidt, S.T. Nguyen, J.T. Hupp, *Chem. Soc. Rev.* 38 (2009) 1450–1459.
- [4] M. Kurmoo, *Chem. Soc. Rev.* 38 (2009) 1353–1379.
- [5] H. Khajavi, J. Gascon, J.M. Schins, L.D. Siebbeles, F. Kapteijn, J. Phys. Chem. C 115 (2011) 12487–12493.
- [6] H. Wang, F. Yin, G. Li, B. Chen, Z. Wang, *Int. J. Hydrogen Energy* 39 (2014) 16179–16186.
- [7] H. Wang, F. Yin, B. Chen, G. Li, J. Mater. Chem. A 3 (2015) 16168–16176.
- [8] S. Ma, G.A. Goenaga, A.V. Call, D.J. Liu, *Chem. Eur. J.* 17 (2011) 2063–2067.
- [9] E. Proietti, F. Jaouen, M. Lefèvre, N. Larouche, J. Tian, J. Herranz, J.-P. Dodelet, *Nat. Commun.* 2 (2011) 416.
- [10] D. Zhao, J.L. Shui, C. Chen, X. Chen, B.M. Reprögle, D. Wang, D.-J. Liu, *Chem. Sci.* 3 (2012) 3200–3205.
- [11] D. Zhao, J.L. Shui, L.R. Grabstanowicz, C. Chen, S.M. Commet, T. Xu, J. Lu, D.J. Liu, *Adv. Mater.* 26 (2014) 1093–1097.
- [12] W. Xia, R. Zou, L. An, D. Xia, S. Guo, *Energy Environ. Sci.* 8 (2015) 568–576.
- [13] Y. Zhang, J. Huang, Y. Ding, *Appl. Catal. B: Environ.* 198 (2016) 447–456.
- [14] P. Zhang, F. Sun, Z. Xiang, Z. Shen, J. Yun, D. Cao, *Energy Environ. Sci.* 7 (2014) 442–450.
- [15] S. Wang, Y. Hou, S. Lin, X. Wang, *Nanoscale* 6 (2014) 9930–9934.
- [16] Y. Gong, Z. Hao, J. Meng, H. Shi, P. Jiang, M. Zhang, J. Lin, *ChemPlusChem* 79 (2014) 266–277.
- [17] J. Mao, L. Yang, P. Yu, X. Wei, L. Mao, *Electrochem. Commun.* 19 (2012) 29–31.
- [18] M. Jahan, Q. Bao, K.P. Loh, *J. Am. Chem. Soc.* 134 (2012) 6707–6713.
- [19] M. Jahan, Z. Liu, K.P. Loh, *Adv. Funct. Mater.* 23 (2013) 5363–5372.
- [20] M.-M. Titirici, R.J. White, N. Brun, V.L. Budarin, D.S. Su, F. del Monte, J.H. Clark, M.J. MacLachlan, *Chem. Soc. Rev.* 44 (2015) 250–290.
- [21] S.S. Gupta, T.S. Sreepasad, S.M. Maliyekkal, S.K. Das, T. Pradeep, *ACS App. Mater. Interfaces* 4 (2012) 4156–4163.
- [22] Y. Zhai, C. Zhu, E. Wang, S. Dong, *Nanoscale* 6 (2014) 2964–2970.
- [23] G. Ruan, Z. Sun, Z. Peng, J.M. Tour, *ACS Nano* 5 (2011) 7601–7607.
- [24] W. Zhen-Yu, L. Chao, L. Hai-Wei, C. Jia-Fu, Y. Shu-Hong, *Angew. Chem.* 125 (2013) 2997–3001.
- [25] L.F. Chen, Z.H. Huang, H.W. Liang, W.T. Yao, Z.Y. Yu, S.H. Yu, *Energy Environ. Sci.* 6 (2013) 3331–3338.
- [26] H. Yao, G. Zheng, W. Li, M.T. McDowell, Z. Seh, N. Liu, Z. Lu, Y. Cui, *Nano Lett.* 13 (2013) 3385–3390.
- [27] C. Peng, X.-b. Yan, R.-t. Wang, J.-w. Lang, Y.-j. Ou, Q.-j. Xue, *Electrochim. Acta* 87 (2013) 401–408.
- [28] W. Huang, H. Zhang, Y. Huang, W. Wang, S. Wei, *Carbon* 49 (2011) 838–843.
- [29] R.J. White, V. Budarin, R. Luque, J.H. Clark, D.J. Macquarrie, *Chem. Soc. Rev.* 38 (2009) 3401–3418.
- [30] S. Gao, K. Geng, H. Liu, X. Wei, M. Zhang, P. Wang, J. Wang, *Energy Environ. Sci.* 8 (2015) 221–229.
- [31] Q. Liang, L. Ye, Z.-H. Huang, Q. Xu, Y. Bai, F. Kang, Q.-H. Yang, *Nanoscale* 6 (2014) 13831–13837.
- [32] J. Zhang, J. Xiang, Z. Dong, Y. Liu, Y. Wu, C. Xu, G. Du, *Electrochim. Acta* 116 (2014) 146–151.
- [33] C. Peng, J. Lang, S. Xu, X. Wang, *RSC Adv.* 4 (2014) 54662–54667.
- [34] P. Chen, L.-K. Wang, G. Wang, M.-R. Gao, J. Ge, W.-J. Yuan, Y.-H. Shen, A.-J. Xie, S.-H. Yu, *Energy Environ. Sci.* 7 (2014) 4095–4103.
- [35] L. Zhou, P. Fu, D. Wen, Y. Yuan, S. Zhou, *Appl. Catal. B: Environ.* 181 (2016) 635–643.
- [36] A.E. Ismanto, S. Wang, F.E. Soetaredjo, S. Ismadij, *Bioresour. Technol.* 101 (2010) 3534–3540.
- [37] G. Saracco, S. Vankova, C. Pagliano, B. Bonelli, E. Garrone, *Phys. Chem. Chem. Phys.* 16 (2014) 6139–6145.
- [38] W. Xia, J. Zhu, W. Guo, L. An, D. Xia, R. Zou, J. Mater. Chem. A 2 (2014) 11606–11613.
- [39] Y. Hou, Z. Wen, S. Cui, S. Ci, S. Mao, J. Chen, *Adv. Funct. Mater.* 25 (2015) 872–882.
- [40] R. Banerjee, A. Phan, B. Wang, C. Knobler, H. Furukawa, M. O’Keeffe, O.M. Yaghi, *Science* 319 (2008) 939–943.
- [41] K.S. Sing, *Pure Appl. Chem.* 57 (1985) 603–619.
- [42] W. Shen, T. Hu, P. Wang, H. Sun, W. Fan, *ChemPlusChem* 79 (2014) 284–289.
- [43] J. Chang, Z. Gao, X. Wang, D. Wu, F. Xu, X. Wang, Y. Guo, K. Jiang, *Electrochim. Acta* 157 (2015) 290–298.
- [44] J. Shui, C. Chen, L. Grabstanowicz, D. Zhao, D.-J. Liu, P. Natl. Acad. Sci. U. S. A. 112 (2015) 10629–10634.
- [45] Z. Kang, M. Xue, D. Zhang, L. Fan, Y. Pan, S. Qiu, *Inorg. Chem. Commun.* 58 (2015) 79–83.
- [46] O. Fleker, A. Borenstein, R. Lavi, L. Benisvy, S. Ruthstein, D. Aurbach, *Langmuir* 32 (2016) 4935–4944.
- [47] L. Ge, Y. Yang, L. Wang, W. Zhou, R. De Marco, Z. Chen, J. Zou, Z. Zhu, *Carbon* 82 (2015) 417–424.
- [48] W. Zhong, H. Liu, C. Bai, S. Liao, Y. Li, *ACS Catal.* 5 (2015) 1850–1856.
- [49] K.-Y.A. Lin, S.-Y. Chen, *RSC Adv.* 5 (2015) 43885–43896.
- [50] J. Li, G. Lu, G. Wu, D. Mao, Y. Guo, Y. Wang, Y. Guo, *Catal. Sci. Technol.* 4 (2014) 1268–1275.
- [51] X. He, F. Yin, G. Li, *Int. J. Hydrogen Energy* 40 (2015) 9713–9722.
- [52] F. Beck, *J. Appl. Electrochem.* 7 (1977) 239–245.
- [53] G. Kuanping, D. Feng, X. Zhenhai, D. Michael, D. Liming, *Science* 323 (2009) 760–764.
- [54] Z.S. Wu, S. Yang, S. Yi, K. Parvez, X. Feng, K. Müllen, *J. Am. Chem. Soc.* 134 (2012) 9082–9085.
- [55] L. Ge, S. Sheng, L. Shao, J.J. Chen, W.J. Bao, F.B. Wang, X.H. Xia, *ACS Nano* 5 (2011) 4350–4358.
- [56] Y. Liang, Y. Li, H. Wang, J. Zhou, J. Wang, T. Regier, H. Dai, *Nat. Mater.* 10 (2011) 780–786.
- [57] H. Zhu, S. Zhang, Y.-X. Huang, L. Wu, S. Sun, *Nano Lett.* 13 (2013) 2947–2951.
- [58] K.N. Wood, R. O’Hayre, S. Pylypenko, *Energy Environ. Sci.* 7 (2014) 1212–1249.
- [59] S. Mao, Z. Wen, T. Huang, Y. Hou, J. Chen, *Energy Environ. Sci.* 7 (2014) 609–616.
- [60] T. Sun, L. Xu, S. Li, W. Chai, Y. Huang, Y. Yan, J. Chen, *Appl. Catal. B: Environ.* 193 (2016) 1–8.
- [61] J. Xiao, Q. Kuang, S. Yang, F. Xiao, S. Wang, L. Guo, *Sci. Rep.* 3 (2013) 2300–2307.
- [62] L. Demarconnay, C. Coutanceau, J.-M. Léger, *Electrochim. Acta* 49 (2004) 4513–4521.

- [63] J. Masa, W. Xia, I. Sinev, A. Zhao, Z. Sun, S. Grütze, P. Weide, M. Muhler, W. Schuhmann, *Angew. Chem. Int. Ed.* 53 (2014) 8508–8512.
- [64] T.Y. Ma, S. Dai, M. Jaroniec, S.Z. Qiao, *J. Am. Chem. Soc.* 136 (2014) 13925–13931.
- [65] L. Wang, C. Lin, D. Huang, F. Zhang, M. Wang, J. Jin, *ACS Appl. Mater. Interfaces* 6 (2014) 10172–10180.
- [66] G. Mattioli, P. Giannozzi, A. Amore Bonapasta, L. Guidoni, *J. Am. Chem. Soc.* 135 (2013) 15353–15363.
- [67] G. Yelena, T.F. Jaramillo, *J. Am. Chem. Soc.* 132 (2010) 13612–13614.
- [68] W. Chaikittisilp, N.L. Torad, C. Li, M. Imura, N. Suzuki, S. Ishihara, K. Ariga, Y. Yamauchi, *Chem. Eur. J.* 20 (2014) 4217–4221.
- [69] X. Fan, Z. Peng, R. Ye, H. Zhou, X. Guo, *ACS Nano* 9 (2015) 7407–7418.
- [70] C.C. McCrory, S. Jung, J.C. Peters, T.F. Jaramillo, *J. Am. Chem. Soc.* 135 (2013) 16977–16987.
- [71] Y. Zhang, X. Bo, C. Luhana, H. Wang, M. Li, L. Guo, *Chem. Commun.* 49 (2013) 6885–6887.